Journal of Non-Newtonian Fluid Mechanics 241 (2017) 26–33

Contents lists available at ScienceDirect

Journal of Non-Newtonian Fluid Mechanics

journal homepage: www.elsevier.com/locate/jnnfm

Rising bubble instabilities and fragmentation in a confined polymer solution

Raphaël Poryles, Valérie Vidal*

Univ. Lyon, ENS de Lyon, Univ. Claude Bernard, CNRS, Laboratoire de Physique, F-69342 Lyon, France

ARTICLE INFO

Article history:
Received 7 August 2016
Accepted 30 January 2017
Available online 1 February 2017

Keywords:
Rising bubbles
Complex fluid
Instabilities
Viscous fingering

ABSTRACT

This work investigates the dynamics of a single bubble rising in a polymer solution confined in a vertical Hele-Shaw cell. Different mixtures of PEO (polyethylene oxide) in water have been used, which exhibit a Newtonian viscosity plateau, followed by a shear-thinning behavior above a shear rate of 0.1 to 1, typically. Depending on the bubble volume, different regimes are reported. When increasing the bubble volume, a transition is observed from a small, round bubble to a cusped bubble, which exhibits a singularity at the rear. Below a critical volume, the bubble rises vertically and does not exhibit any apparent shape deformation. However, above a critical volume, the cusped bubble develops a peculiar instability. Its front flattens at a given angle respect to the horizontal, leading to either a deflection in its trajectory, or its fragmentation. We characterize these two dynamics and interpret the fragmentation process in terms of a viscous fingering recalling the Saffman–Taylor instability. Interestingly, the finger growth is directly controlled by the bubble size.

1. Introduction

Bubbles rising in non-Newtonian fluids exhibit a wide range of puzzling behaviors which have excited different research communities for decades. Indeed, they are widely encountered in nature, from degassing on the ocean floor [1,2] to giant bubbles rising and bursting on volcanoes [3–6]. In both cases, the complex nature of the surrounding fluid (soft immersed sediments, bubble- or crystal-rich magma [1,7–9]) give rise to non-Newtonian effects, such as shear-thinning behavior [9,10]. This effect strongly couples to the bubble rise dynamics and often makes it difficult to interpret the field data. From a more fundamental point of view, experimental studies of bubbles rising in non-Newtonian fluids have started in the 60's, leading to a large amount of either experimental or numerical works which strongly developed since the 80's [11]. Among the many peculiar observations are the deformation of the bubble shape respect to Newtonian fluids [12–14], the presence of a singularity at the bubble rear (cusp) [11,15] and a negative wake due to elastic properties [16], oscillations of the bubble shape or velocity [17,18], or the existence of a discontinuity in the bubble terminal velocity for a critical volume [19,20]. All these phenomena have been reported for bubbles rising in unconfined non-Newtonian fluids.

On the other hand, the influence of fluid confinement can have drastic consequences on the bubbles dynamics and, more generally, on the gas invasion dynamics in viscous fluids. The pioneer study is the classical Saffman–Taylor problem, consisting in the injection of air at constant pressure in a horizontal quasi two-dimensional cell (Hele-Shaw cell) filled with a Newtonian, viscous fluid [21,22]. It has been shown that the initially planar interface deforms, leading to the growth of a finger-like instability, which has been widely studied theoretically [23] and experimentally [24]. More recent studies considered the Saffman–Taylor instability in the case of non-Newtonian fluids. They pointed out that for weakly shear-thinning fluids (dilute polymer solutions), using an effective Darcy's law with the shear-thinning viscosity accounts for the finger width [25]. For strong shear-thinning fluids, narrower fingers are reported [25]. When the fluid exhibits normal stress effects rather that shear-thinning effects, however, the experiments show a finger widening [26,27].

Although apparently simple, the problem of a single bubble rising under its own buoyancy in a confined, non-Newtonian fluid has not been tackled yet. Even the simpler case of a single bubble rising in a viscous, Newtonian fluid such as water, mentioned by Taylor and Saffman since 1959 [28], is still investigated nowadays [29–31]. In particular, most studies focus on the triggering of path instabilities, an oscillatory bubble motion observed either in confined or unconfined cell, and which triggering depends on the fluid rheology [32–35].

* Corresponding author.
E-mail address: valerie.vidal@ens-lyon.fr (V. Vidal).

http://dx.doi.org/10.1016/j.jnnfm.2017.01.006
0377-0257/

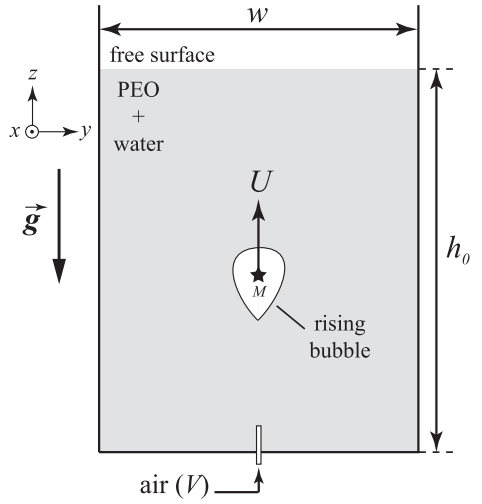

Fig. 1. Sketch of the experimental setup. A single bubble (volume V) is injected at the bottom of a vertical Hele-Shaw cell of width w, filled with a PEO + water solution up to a height h_0. It rises with a vertical velocity U. Its center of mass is M [black star, coordinates (y_M, z_M)].

Here, we present the experimental study of a single bubble rising in a vertical Hele-Shaw cell. The surrounding fluid is a solution of long polymer chains (see Section 2.2), characterized by a strong shear-thinning behavior. The polymer concentration is chosen high enough so that (1) non-Newtonian effects are significant and (2) the local viscosity is always high enough to prevent the formation of the classical path instabilities. We report a new type of instability (Section 3), leading to either the bubble horizontal deflection or fragmentation.

2. Experimental setup

2.1. Description

The experimental setup consists of a Hele-Shaw cell made of two glass plates (width $w = 28.3$ cm, height 40 cm, gap $e = 2$ mm), which are systematically removed and carefully cleaned with water, ethanol and optical paper before each series of experiments. The cell is then filled with a polymer solution (see Section 2.2) up to a height $h_0 \simeq 30$ cm (Fig. 1). Air is injected manually through a nozzle (inner diameter 1 mm) by means of a syringe (capacity 60 mL). By tuning the amplitude and velocity of the injection, the volume V of the single injected bubble can be varied, typically between 0.01 and 1.5 mL (see Section 2.3). After the injection, the bubble rises by buoyancy. We denote U its vertical velocity and M its center of mass [coordinates (y_M, z_M)] (Fig. 1). The origin of the coordinates (0, 0) is taken at the injection nozzle, at the bottom center of the cell.

A homogeneous backlight is ensured by a transparency flat viewer (Just NormLicht, Classic Line) located behind the cell. Direct visualization of the bubble dynamics is performed using a video camera (PixeLink PL-B781) with an adjustable lens (12.5–75 mm with a focal distance of 1.2 m), a resolution of 1280 × 416 pixels and a frame rate of 41 fps.

2.2. Fluids characterization

The fluids used in these experiments are polymer solutions of polyethylene oxide (PEO) in water. The PEO is sold as a white powder which can be diluted in water at different concentrations, making it possible to tune the rheological properties of the mixture [PEO+water]. It is characterized by a high molecular weight, $M_w = 8 \times 10^6$ g/mol (Sigma-Aldrich, 372838). For polymer solutions, one can define the entanglement concentration of the polymer chains as

$$C^* = \frac{M_w}{(4/3)\pi R_g^3 \mathcal{N}_a}, \quad (1)$$

where M_w is the molecular weight, R_g the gyration radius of the polymer and $\mathcal{N}_a$ the Avogadro number [36]. For the PEO described above, the entanglement concentration is $C^* = 0.04$ g/L. Four different polymer solutions were prepared with the following concentrations: $c = [75, 100, 125, 150]C^*$, corresponding to $c = [3, 4, 5, 6]$ g/L. These high concentrations ensure that (1) the polymeric chains are well-entangled, (2) the viscosity is higher than the water viscosity and (3) the non-Newtonian effects will be non-negligible in our experiment. The value of the surface tension has been measured using a commercial tensiometer (Tracker, Teclis) based on the rising bubble technique, equivalent to the pendant drop [37,38]. For the solution at $c = 100C^*$, the surface tension is $\sigma = 64 \pm 2$ mN/m. It is assumed to be the same for all the polymer solutions.

The rheological properties of the polymer solutions have been characterized by a rheometer (Bohlin C-VOR 150) with a cone-plane geometry (diameter 60 mm, angle 2°). Fig. 2a displays the fluids dynamic viscosity η as a function of the applied shear rate $\dot{\gamma}$. The four polymer solutions exhibit a viscosity between about 10–1000 times the viscosity of water, and a shear-thinning behavior above a critical shear rate $\dot{\gamma}_c$, in agreement with previous studies on PEO solutions rheology [39]. Note that $\dot{\gamma}_c \simeq 0.1$–$1\ s^{-1}$, of the order of magnitude of the shear rates in our experiments.

The shear-thinning behavior of entangled flexible polymers has been often modeled by the Carreau law, which takes into account both the Newtonian plateau at low shear rate and the decreasing slope at higher shear-rate [40]. However, we observe slight differences in the decreasing slope for the different concentrations, which is not compatible with the power $-1/2$ predicted by this simple law. Here, we use the more generalized Carreau–Yasuda law [41]

$$\eta = \eta_\infty + \frac{\eta_0 - \eta_\infty}{[1 + (\tau\dot{\gamma})^a]^{\frac{1-n}{a}}} \quad (2)$$

where η_0 is the viscosity at zero shear rate, η_∞ the viscosity at infinite shear rate (or solvent viscosity), τ a characteristic time, n a dimensionless exponent and a a dimensionless parameter describing the transition between the first Newtonian plateau and the shear-thinning region [41]. For all the solutions, the solvent is water and $\eta_\infty = 10^{-3}$ Pa s. Table 1 summarizes the fitting parameters (η_0, τ, n, a) for the PEO solutions of different concentrations (see gray lines in Fig. 2).

Table 1
Parameters of the Carreau–Yasuda law fitting the rheology of the four PEO solutions (see gray lines, Fig. 2).

c [g/L]	η_0 [Pa s]	τ [s]	n [-]	a [-]
3	0.12	0.69	0.59	2.76
4	0.49	1.92	0.52	2.04
5	1.37	4.19	0.48	2.02
6	4.12	6.09	0.40	1.12

Fig. 2b displays the first normal stress coefficient, $\psi_1 = N_1/\dot{\gamma}^2$, where N_1 is the first normal stress difference for the four PEO solutions. For PEO solutions, the first normal stress difference is predicted to increase quadratically with the shear rate [42]. However, a less-that-quadratic behavior is observed with ψ_1 decreasing with $\dot{\gamma}$, as already reported for PEO-water mixtures and within the same order of magnitude than in the literature [39].

The viscoelastic properties of the fluids have been measured with a rheometer TA Instruments, AR100 with a cone-plate geometry of diameter 40 mm, angle 2°. Fig. 2c displays the elastic

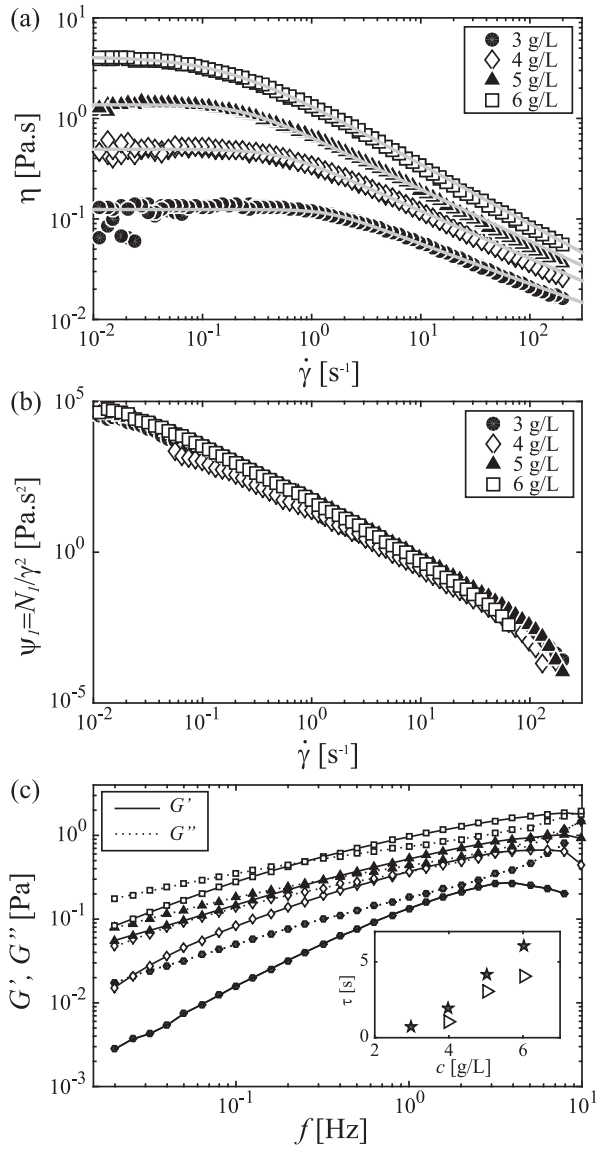

Fig. 2. (a) Viscosity η as a function of the imposed shear rate $\dot{\gamma}$ for the polymer solutions [$c = 3,4,5,6$ g/L]. Measurements are performed for increasing and decreasing $\dot{\gamma}$ [waiting time $\Delta t = 10$ s per point]. No hysteresis is reported. The gray lines correspond to the Carreau–Yasuda law (see Eq. (2) and Table 1 for fitting parameters) (b) First normal stress difference coefficient, $\psi_1 = N_1/\dot{\gamma}^2$ as a function of $\dot{\gamma}$. (c) Elastic (G', solid lines) and viscous (G'', dashed lines) modulii as a function of frequency [$\gamma = 1$, same symbols than (a,b)]. *Inset:* Relaxation time τ from the Carreau–Yasuda model [⋆, see (a) and Table 1] and from the viscoelastic properties (crossover, ▷).

(G') and viscous (G'') modulii obtained by performing a frequency sweep for the four concentrations at fixed strain $\gamma = 1$, corresponding roughly to the strain order of magnitude in our experiments. The fluids relaxation time (inset, Fig. 2c) can be extracted either from the Carreau–Yasuda fitting (τ, Table 1) or from the crossover between the G' and G'' curves (τ_{ve}, Fig. 2c). Both estimations are close, going from about 0.7 s to 6 s from the lowest to the highest concentration. Note that the value of τ_{ve} does not change significantly when performing a frequency sweep at $\gamma = 0.1$.

For sake of comparison, we conducted experiments with a purely Newtonian liquid, consisting of a mixture of glycerol and water of viscosity 0.1 Pa s. This viscosity has been chosen to match the average viscosity experienced by a bubble rising in the $c =$ 4 g/L solution, where $\dot{\gamma}$ can be estimated of the order of 1–10 s^{-1} for our experimental range of bubble size and velocity.

2.3. Bubble volume

As the bubble injection is hand-made (see Section 2.1), it is *a priori* difficult to control precisely its volume. However, the goal here is to explore a wide range of volumes, without any pre-established order, and to cover the whole range available. To do so, for each polymer solution, more than 200 bubbles have been analyzed. Note that after each bubble rise and subsequent burst at the surface, the fluid is let at rest for a couple of minutes. Indeed, due to the fluid shear-thinning behavior, the rising bubble generates a corridor of reduced viscosity in its wake (see for instance [18]). Waiting for the fluid to rest and recover its initial viscosity after each bubble ensures that all bubbles rise in the same experimental conditions. The bubble size is varied by tuning the amplitude and velocity of the injection, and its volume V is determined *a posteriori*.

When a bubble pushes a confined wetting liquid, it has been shown that the lubrication layer thickness h can be written [43]

$$\frac{h}{e} \sim \frac{Ca^{2/3}}{1 + Ca^{2/3}} \tag{3}$$

where $Ca = \eta U/\sigma$ is the capillary number, with η the fluid dynamic viscosity, U the bubble velocity and σ the surface tension. In all our experiments, the capillary number is in the range $Ca \simeq$ [0.01–0.1], thus $h/e \sim Ca^{2/3} \ll 1$. As the lubrication layer thickness is much smaller than the cell gap e, the bubble volume can therefore be computed as $V \simeq S.e$, where S is the apparent surface of the bubble. This latter is determined directly from the images, by a simple contour detection. We therefore explore bubble volumes ranging from 0.01 and 1.5 mL. The center of mass of the bubble, M [coordinates (y_M, z_M)] (Fig. 1), is computed from the images. The bubble vertical speed U is obtained by a linear fit of $z_M(t)$ over the central part of the cell, ignoring the regions close to the injection nozzle (transient regime) and close to the surface (where the bubble slows down).

3. Different regimes

For the PEO concentrations $c = 4, 5, 6$ g/L, we report three different regimes for the bubble shape and dynamics, depending on the bubble volume. The volumes indicating the transition between the different regimes in the following are given for the $c = 4$ g/L solution, as an example.

(1) For small volumes ($V < 0.1$ mL), the capillary forces are predominant and the bubbles exhibit a round shape (Fig. 3a); they rise vertically, without any apparent deformation in their shape, at constant velocity U along most of their path (except right at the injection nozzle and close to the fluid free surface).

(2) When increasing the volume ($0.06 < V < 0.65$ mL), the bubbles still follow a straight, vertical trajectory but display a cusp at their rear (Fig. 3b). The existence of an apparent cusp at the trailing end of a rising bubble has been widely reported in 3D experiments, where the bubble rises freely in a non-confined viscoelastic fluid (see for instance [11,15,40]). It has been pointed out as a consequence of the fluid viscoelastic properties, which generate a negative wake at the bubble rear and leads to its teardrop shape [15,16,44]. Note that in this regime, the bubble still follows a vertical trajectory, and does not display any shape deformation during its rise. Note also that there is an overlap with the round bubble regime ($0.06 < V < 0.1$ mL).

(3) Above a critical volume ($V > 0.65$ mL), the bubble deforms, departs from its vertical trajectory, and we report two instabilities. Either the bubble deforms preferentially on one side (Fig. 3c), and displays a lateral deflection before recovering

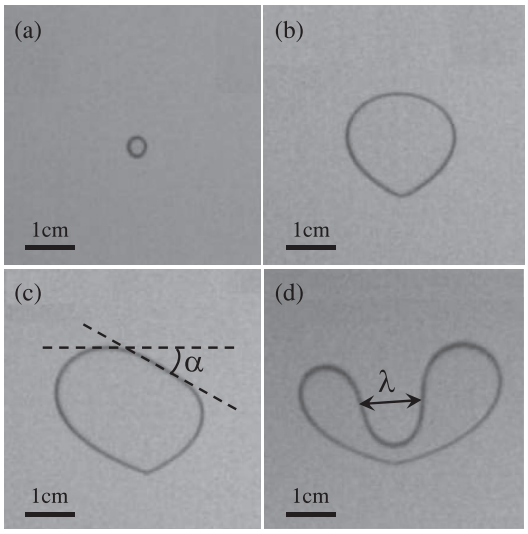

Fig. 3. Different regimes observed when increasing the bubble volume [here, $c = 4$ g/L]. (a) Small circular bubble [$V = 0.02$ mL]; (b) bubble exhibiting a cusp at its rear [$V = 0.57$ mL]; (c) bubble deflection (note the flat front at angle α, see text) [$V = 0.89$ mL]; (d) bubble fragmentation with a fingering instability of typical width λ [$V = 0.84$ mL]. The bubbles in the upper panel (a,b) rise vertically, while the bubbles in the lower panel (c,d) exhibit either a horizontal deflection in their trajectory (c) or a fragmentation (d).

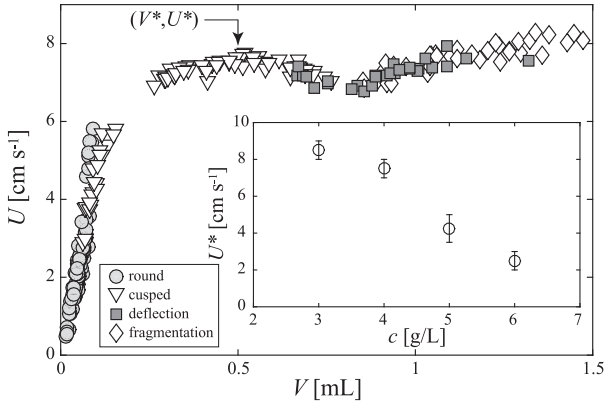

Fig. 4. Vertical velocity of the bubble U as a function of its volume V [$c = 4$ g/L, (◯, round bubbles), (▽, cusped bubbles rising vertically), (□, deflected bubbles), (◇, fragmenting bubbles)]. *Inset:* velocity U^* of bubbles with a fixed volume $V^* = 0.5$ mL as a function of the concentration.

a vertical trajectory, or a finger develops at the bubble front (Fig. 3d), leading to the bubble fragmentation. These instabilities are not triggered at fixed locations in the experimental cell, and are therefore not due to the possible presence of impurities on the glass plates. The dynamics of both instabilities is further described in Section 4. Note that, once again, there is a slight overlap between the bubbles displaying a deflection and the cusped bubbles rising vertically ($0.65 < V < 0.75$ mL).

For the lowest concentration ($c = 3$ g/L), the third regime has to be interpreted with caution. Indeed, for this solution, the viscosity is low and inertial instabilities appear, which superimpose to the deflection or fragmentation instabilities. The bubble shape fluctuates, but does not display either clear oscillations as in the case of path instabilities due to the interaction between the bubble rise and the Kármán vortex generated in its wake, either in simple or complex fluids [32,34,35]. Because these inertial instabilities are not clearly identified, in the more detailed description of the deflection and fragmentation instabilities (Section 4.2) we will not consider this lower concentration.

In the reference experiment with the purely Newtonian fluid (water-glycerol mixture), the bubbles have a round or elongated shape but do not exhibit any deflection instability. They rise vertically with a velocity up to 6 cm/s for the largest bubbles, of the same volume than the largest bubbles in the PEO experiment ($V \simeq 1.5$ mL). For even larger bubbles, generated by pushing quickly on the syringue, we do observe a fragmentation, as the capillary forces are not sufficient anymore to maintain the bubble shape. However, this fragmentation occurs immediately during the bubble formation at the nozzle, and therefore cannot be compared to the mechanism of flat front development reported for PEO solutions. This confirms that the origin of the instability previously described lies in the non-Newtonian properties of the fluid. Fig. 4 displays the evolution of the bubble vertical velocity, U, as a function of its volume V, for $c = 4$ g/L. Two regimes are reported: for low volumes ($V < 0.2$ mL), the bubble velocity is proportional to its volume; then the increase is much smaller, and the velocity reaches roughly a plateau, although the cusped bubbles motion is still purely vertical (up to 0.5–0.6 mL). The minimum observed around 0.8 mL can be explained by the fact that the bubbles now exhibit instabilities (deflection or fragmentation), meaning that their velocity is not purely vertical and thus, in absolute, larger that U. The vertical velocity variations as a function of volume are similar for the other PEO concentrations, the curves are only shifted towards lower velocities when the concentration increases, in agreement with the viscosity increase with respect to the concentration (see Fig. 2). We define (V^*, U^*) as the critical volume and velocity for which the bubble reaches the vertical velocity plateau, which is arbitrarily set at $V^* = 0.5$ mL (black arrow, Fig. 4). Fig. 4, inset, shows the evolution of the critical velocity U^* as a function of the PEO concentration. We report a strong decrease, going from $U^* \simeq 8$ cm s^{-1} for $c = 3$ g/L to $U^* \simeq 2$ cm s^{-1} for $c = 6$ g/L.

Note that we do not observe, in confined experiments, the terminal velocity discontinuity observed when bubbles of increasing volume rise in non-Newtonian, unconfined liquids [19,20]. This latter has been interpreted in terms of a transition between the Stokes to the Hadamard-Rybczinski regime [19], or the appearance of the so-called negative wake behind the bubble [16,20]. Although a gap exists in the data (no data points between 0.15 and 0.26 mL in Fig. 4), it cannot be interpreted as a discontinuity. In the specific experiment at $c = 4$ g/L, it is due to the bubble injection method: large bubbles are generated by pushing quickly on the syringe, resulting in the coalescence of small bubbles close to the injection nozzle. We therefore observe a gap between the small bubbles ($V < 0.2$ mL) generated individually and the larger bubbles ($V > 0.25$ mL) generated by smaller bubbles coalescence. In the next section, we will focus on the description of the instabilities occurring when the bubble is above a critical volume, and exhibits either a deflection or a fragmentation.

4. Analysis of the instabilities

4.1. Instability threshold

Here, we characterize the transition between the cusped bubbles, rising vertically, and the bubbles displaying an instability (deflection or fragmentation). From the data presented in Fig. 4, it is possible to quantify the volume and velocity above which the bubbles exhibit an instability for each PEO concentration. To characterize the transition, we introduce two dimensionless numbers which describe the forces at stake in the system. First, the Reynolds number compares the inertial forces to viscous forces, $Re = uL/\nu$, where u and L are a typical velocity and length scale, respectively, and $\nu = \eta/\rho$ the kinematic viscosity, with $\rho \simeq 1000$ kg m^{-3}

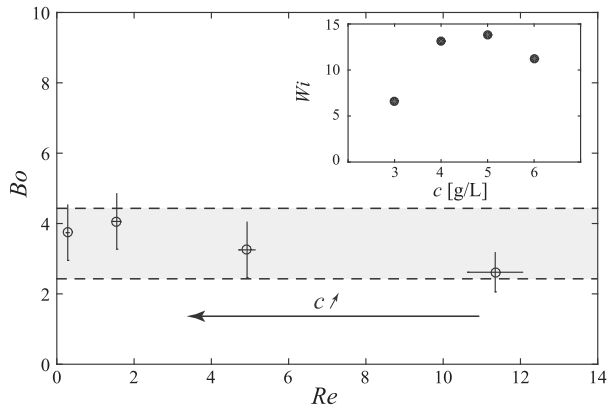

Fig. 5. Bond number as a function of the Reynolds number at the transition between bubbles rising vertically and bubbles exhibing an instability (deflection or fragmentation). The black arrow indicates the evolution of the PEO concentration [$c = 3, 4, 5, 6$ g/L]. *Inset:* Weissenberg number *Wi* at the transition as a function of the PEO concentration c (see text).

the fluid density. Then, due to the importance of capillary forces in the system, we introduce the Bond number (or Eötvös number), which compares buoyancy to surface tension forces, $Bo = \Delta\rho g L'^2/\sigma$, where $\Delta\rho \simeq \rho$ is the density difference between the air in the bubble and the surrounding fluid, $g = 9.81$ m^2 s^{-2} is the gravitational acceleration, L' a typical length and σ the surface tension. For estimating these numbers, the difficulty arises in choosing the right length scales, as well as the viscosity - which, we remind, strongly varies with the shear rate, *i.e.* with the bubble size and velocity.

For the Reynolds number estimation, the following scales are chosen: $u \sim U$, the bubble velocity; $L \sim r = \sqrt{S/\pi}$, the bubble equivalent radius estimated from its apparent surface, S, and $\eta = \eta(\dot\gamma)$, where $\dot\gamma \simeq U/r$ is the typical shear rate.

$$Re \sim \frac{\rho U r}{\eta(\dot\gamma)} \tag{4}$$

where $\eta(\dot\gamma)$ is estimated from each PEO rheology (see Fig. 2 and Table 1). For the Bond number estimation, note that two length scales are at stake. Indeed, the buoyancy forces depend directly on the volume, which can be estimated here as $V \simeq S.e$ (see Section 2.3), and $S \sim r^2$, which leads to

$$Bo \sim \frac{\rho g e r}{\sigma} \tag{5}$$

Fig. 5 displays the Bond vs. Reynolds number at the instability threshold for the four PEO concentrations. Despite small variations, the Bond number is roughly constant at the transition, $Bo \simeq 3.5 \pm 1$, although the Reynolds number varies strongly, from $Re = 11.3$ for $c = 3$ g/L to $Re = 0.3$ for $c = 6$ g/L. This result tends to indicate that the transition is controlled by the Bond number, i.e. mainly by the bubble size, r. The point for $c = 3$ g/L has to be interpreted with caution. Indeed, even if the bubbles exhibit a transition between a stable teardrop shape rising vertically and the appearance of instabilities, these latter are coupled to inertial instabilities deforming the bubble shape (see Section 3). The independence of the transition on the Reynolds number is further discussed in Section 5.

Because the PEO solutions are viscoelastic (see Section 2.2), one can wonder if the Weissenberg number, comparing the elastic and viscous forces, may be a better parameter to explain the appearance of instabilities. We thus estimate the Weissenberg number by

$$Wi = \tau\dot\gamma \tag{6}$$

where τ is a typical fluid relaxation time and $\dot\gamma \simeq U/r$ the typical shear rate [45–47], with U and r the velocity and radius of the bubble at the transition. As previously, the difficulty arises in estimating the right parameters, in particular the relaxation time, as a polymeric liquid is generally characterized by a large spectrum of relaxation times [46]. Here, we take τ as the relaxation time estimated with the Carreau–Yasuda model (see Section 2.2, Fig. 2c, inset and Table 1), as already proposed in previous work [44]. The Weissenberg number is typically between 5 and 15 (Fig. 5, inset), indicating a non-negligible elastic component. However, its variation is large at the transition, and its value does not indicate a predominance of elastic forces respect to viscous forces right at the appearance of the instabilities. The Bond number is therefore a better candidate to control the triggering of the instabilities.

4.2. Deflection vs. fragmentation

In Fig. 6, two sequences of images show the bubble dynamics during the deflection or fragmentation process. Contrary to the bubbles of smaller volumes (round or cusped bubbles), the bubble deforms as follows. First, it develops a flat front at its head. This flat front can develop at any location in the experimental cell and exhibits an apparently random angle, α, respect to the horizontal (Fig. 3c). In all experiments, no value of α larger than 40° was reported. The behavior of the bubble – deflection or fragmentation – is directly related to the front angle α.

For $\alpha > 10°$, the bubble trajectory is systematically deviated in the direction opposite to the flat front (Fig. 6c–g, upper panel). It experiences a lateral motion, before recovering its initial shape (Fig. 6h, upper panel). After the deflection, it rises vertically over some distance, before developing a flat front again. Note that the motion is not oscillatory. Indeed, the flat develops randomly on either side of the bubble, which can exhibit successive deflections without any periodic alternance. An example of the temporal evolution of the horizontal position of the bubble center of mass, y_M, can be seen in Fig. 7, inset, where the bubble experiences four deflections along its rise, one towards $y > 0$, two towards $y < 0$ and the last one towards $y > 0$. The reference $y = 0$ is taken here at the vertical of the injection nozzle.

For $\alpha < 4°$, the bubble dynamics is always a fragmentation, which occurs via the growth of a fingering instability on the bubble front (Fig. 6, lower panel). In this case, the capillary forces are not enough to maintain the bubble as a whole, the finger grows until reaching the rear of the bubble (Fig. 6g, lower panel), which then fragments into two smaller bubbles (Fig. 6h, lower panel). Note that these smaller bubbles can further experience deflection or fragmentation if their volume is large enough. In the intermediate range ($4 \leq \alpha \leq 10°$), the deflection and fragmentation phenomena overlap, and we cannot predict *a priori* the bubble dynamics.

Fig. 7 displays the horizontal deviation Δy of the deflected bubbles as a function of the absolute value of the front angle which develops at the beginning of the deflection instability, $|\alpha|$. Δy here represent the absolute value of the horizontal motion, and is normalized by the bubble equivalent radius, r (see Section 4.1). The figure therefore compiles deflections towards both $y > 0$ and $y < 0$. The gray zone for $|\alpha| < 4°$ represents the small values of the front angle for which the bubble systematically fragments. The horizontal motion of deflected bubbles ($|\alpha| > 4°$) is always of the order of or smaller than their equivalent radius, and varies between 20% (for $\alpha \sim 35°$) and 100% (for $\alpha \sim 4°$) of this latter. Although the experimental points are scattered, the data can be roughly adjusted by a parabolic shape, $\Delta y/r - 1 = \xi\alpha^2$, where $\xi \simeq 6.5 \times 10^{-4}$.

In the case of bubble fragmentation, we focus on the instability growing from the bubble front towards the bubble tail (see Fig. 6, lower panel, d–g). This finger-like instability can be characterized by the typical width of the finger, measured at half height, when is it fully developed (Fig. 3d). It is tempting to make an analogy with the classical Saffman–Taylor instability, where a finger devel-

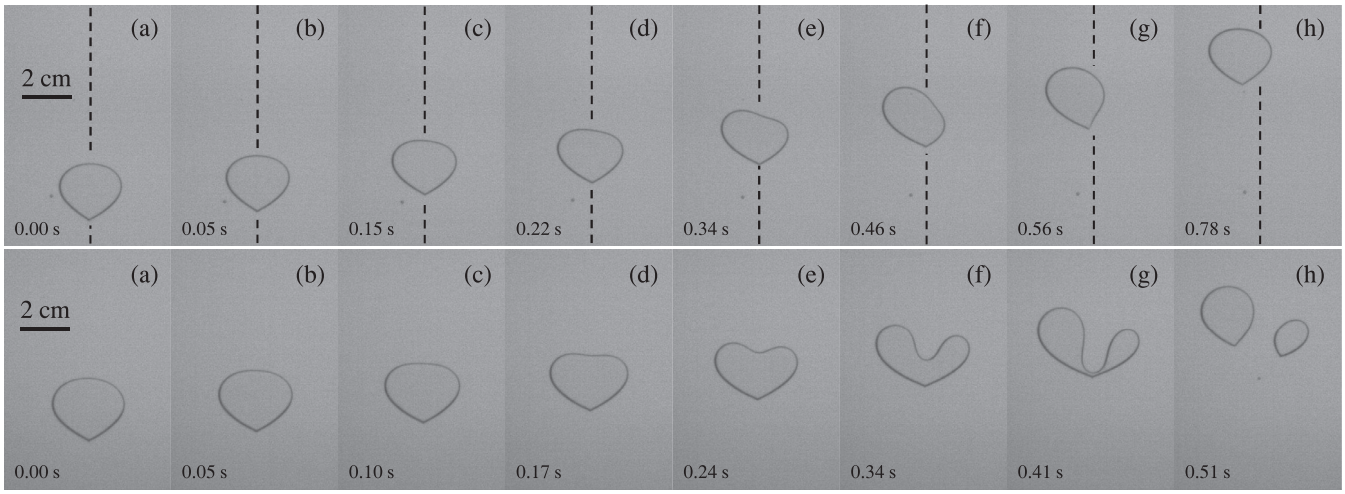

Fig. 6. Sequence of images for a rising bubble exhibiting a deflection (*upper panel*, $V = 1.0$ mL) or fragmenting (*lower panel*, $V = 1.1$ mL) [c=4 g/L]. The time relative to the first image (a) is indicated on the images (a–h). The black dashed line in the upper panel indicates the vertical trajectory of the rising bubble before its deflection. The images from the upper and lower sequences have been cropped to zoom on the bubbles and do not correspond to the same location in the experimental cell.

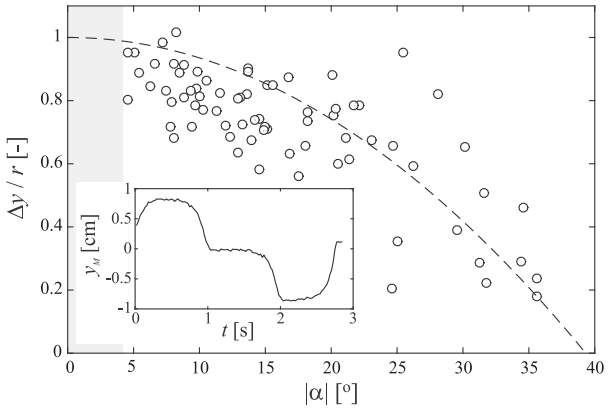

Fig. 7. Horizontal motion of the deflected bubbles, Δy, normalized to the bubble equivalent radius, r, as a function of the absolute value of the angle of the flat front, $|\alpha|$ [$c = 4$ g/L]. The gray zone indicates the region $\alpha < 4°$, in which the bubbles fragment. The dashed line is a parabolic fit of the data (see text). *Inset:* Example of the horizontal position y_M of the bubble center of mass for a deflected bubble. Note that the motion is not oscillatory, the deflection here being one right (towards $y > 0$), twice left (towards $y < 0$) then one right again (towards $y > 0$).

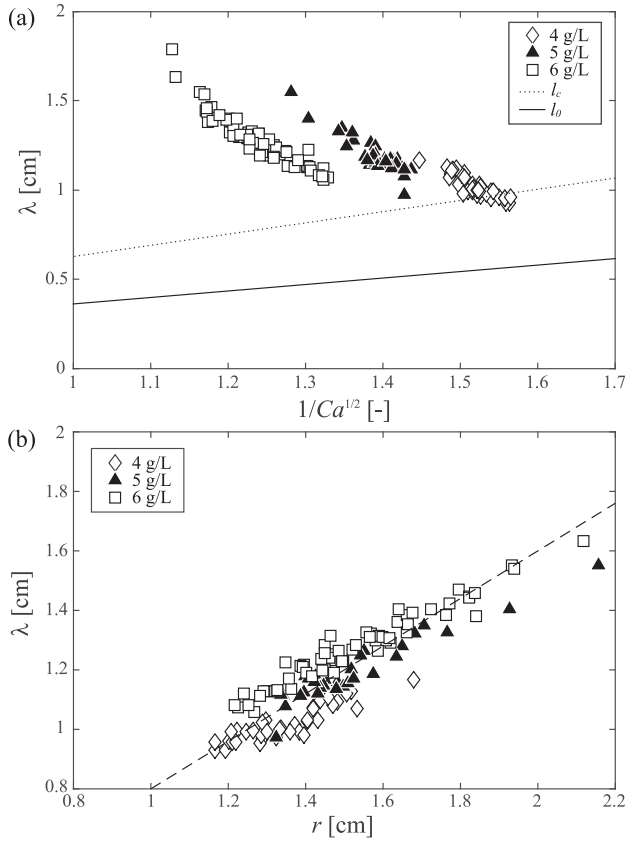

Fig. 8. (a) Finger width λ (defined in Fig. 3d) as a function of $1/Ca^{1/2}$ for fragmenting bubbles, for the different PEO concentrations. The full and dotted lines represent the linear stability analysis for Newtonian fluids in the classical Saffman–Taylor problem (see text). (b) λ as a function of the bubble equivalent radius, $r = \sqrt{S/\pi}$, for the different PEO concentrations. The dashed line is the linear fit for all concentrations, $\lambda \simeq 0.80\, r$.

ops when a less viscous fluid is pushed into a more viscous fluid in a Hele-Shaw cell [21,22]. A linear stability analysis, for the simple case of Newtonian fluids, shows that the Saffman–Taylor finger growth rate is positive for $l > l_0$, where l is the wavelength, with a maximum growth rate for $l_c = \pi e/\sqrt{Ca}$, and $l_0 = l_c/\sqrt{3}$ [48]. Here, $Ca = \eta U/\sigma$ is the capillary number. Note that if the bubble is too small, $l < l_0$ and the instability will not develop, in agreement with the observations. Fig. 8a displays the width λ of the finger obtained in our experiments as a function of $1/Ca^{1/2}$, as predicted for the Newtonian fluid theory. To be consistent, Ca is computed as $Ca = \eta(\dot\gamma)U/\sigma$, where $\dot\gamma \sim U/r$ (see Section 4.1) and $\eta(\dot\gamma)$ is estimated from the PEO rheology (Fig. 2 and Table 1). Although it is consistent with $\lambda > l_0$, the finger width does not match with $\lambda = l_c$, meaning that the non-Newtonian effects are important for these polymer concentrations, and cannot be explained by a simple modification of Darcy's law [27]. For high polymer concentrations and strong non-Newtonian effects, previous studies have pointed out either a finger narrowing, when shear-thinning effects are dominant, or finger widening, when normal stress effects are dominant [26,27]. The experimental results displayed in Fig. 8 tend to show a finger width larger than the Newtonian prediction. This result is consistent with the fact that the Weissenberg number Wi is larger than 1 when the instabilities are observed in our experiments (see Section 4.1). However, these results have to be interpreted with caution. Indeed, on the one hand, the capillary num-

ber has been estimated with a typical bubble velocity and radius. The choice of U and L (here, $L \sim r$, the bubble equivalent radius) may affect the estimation of Ca. On the other hand, let us remember that our experimental configuration is far from the classical instability of an infinite interface as in the Saffman–Taylor problem. Note that, finally, the width of the finger does not seem to depend much on the PEO concentration, and always ranges between $\lambda \simeq 1$ and 2 cm.

A more straightforward dependence is found by plotting λ as a function of the bubble equivalent radius, $r = \sqrt{S/\pi}$. All the data roughly collapse on a straight line, leading to $\lambda \simeq 0.80r$, independently of the PEO concentration. This results points out that the bubble size is the dominant parameter controlling the fingering instability.

5. Discussion and conclusion

Bubbles rising in a confined polymer solution develop instabilities when their volume is larger than a critical volume. This instability leads either to the bubble fragmentation, with the formation of a finger growing until reaching the bubble tail, or to a peculiar horizontal deflection of the bubble trajectory. Similar experiments made with a Newtonian fluid, a water-glycerol mixture with $\eta = 0.1$ Pa s, matching the average viscosity experienced by the bubble for the PEO solution at $c = 4$ g/L, did not display any bubble deflection, although fragmentation can be observed for very large volumes - larger that the range used in the PEO experiments. In this last case however, the fragmentation mechanism does not result from the bubble rise and development of a flat front, but from a transient process where capillary forces are not sufficient anymore to maintain the bubble shape at the injection.

The instabilities appearance is almost independent of the Reynolds number. This independence has been previously reported in the case of path instabilities of bubbles in Newtonian fluids, where the bubble shape, and not the Reynolds number, was found as the dominant parameter to trigger the instability [33]. Although the nature of the instabilities and the experimental conditions are different, it is interesting to point out that in both cases, the instabilities seem to be driven by the bubble shape rather than its inertia. Indeed, this work points out that the Bond number is the possible dimensionless parameter responsible for the triggering of the instability, while the finger width in the case of bubble fragmentation is directly controlled by the bubble size.

The physical mechanism at the origin of the instabilities, however, still remains unknown. Because the instabilities are not observed for the water-glycerol solutions, their possible origin lies in the non-Newtonian properties of the fluid. Although elastic effects and normal stresses are non-negligible, they do not seem to directly control the instability threshold. As a tentative explanation, we propose that the existence of the flat front, which leads to the instability development, is due to the fluid strong shear-thinning properties. Indeed, as the fluid is shear-thinning, the local viscosity is smaller on the sides of the bubble, where the larger shear locates, than on its front, as was previously reported in 3D experiments [49]. Hence, the bubble sides have a tendency to rise faster that its front, causing the observed flattening at an angle α. If α is large enough (typically, $\alpha > 4°$), the bubble deviates from its trajectory, and the capillary forces are enough to prevent its fragmentation. The lateral deviation, normalized by the equivalent bubble radius, follows a decreasing parabolic trend as a function of α. No explanation has been found at present for this behavior. If $\alpha < 4°$, a phenomenon analogous to viscous fingering occurs. The capillary forces are not strong enough to prevent the finger growth, until it reaches the bubble tail and leads to the bubble fragmentation. An overlap is reported between deflection and fragmentation for $4 < \alpha < 10°$.

To confirm the above explanation, further work would be necessary to separate shear-thinning and elastic effects. Previous studies on bubbles ascending in shear-thinning, inelastic fluids in non-confined columns pointed out the importance of shear-thinning effects on the bubbles hydrodynamics [50,51], which could support the origin of the instabilities in the confined geometry.

Acknowledgments

The authors acknowledge the editor and two anonymous referees for their comments which greatly helped in improving the manuscript, especially concerning the PEO rheological characterization and the role of normal stresses.

References

[1] B.P. Boudreau, C. Algar, B.D. Johnson, I. Croudace, A. Reed, Y. Furukawa, K.M. Dorgan, P.A. Jumars, A.S. Grader, B.S. Gardiner, Bubble growth and rise in soft sediments, Geology 33 (6) (2005) 517–520.
[2] C. Bourry, B. Chazallon, J.L. Charlou, J.P. Donval, L. Ruffine, P. Henry, L. Gely, M.N. Çagatay, S. Inan, M. Moreau, Free gas and gas hydrates from the Sea of Marmara, Turkey. chemical and structural characterization, Chem. Geol. 264 (2009) 197–206.
[3] S. Vergniolle, G. Brandeis, Origin of the sound generated by Strombolian explosions, Geophys. Res. Lett. 21 (18) (1994) 1959–1962.
[4] S. Vergniolle, G. Brandeis, Strombolian explosions 1. A large bubble breaking at the surface of a lava column as a source of sound, J. Geophys. Res. 101 (B9) (1996) 20433–20447.
[5] M. Ripepe, E. Gordeev, Gas bubble dynamics model for shallow volcanic tremor at Stromboli, J. Geophys. Res. 104 (B5) (1999) 10639–10654.
[6] K.R. Jones, J.B. Johnson, R. Aster, P.R. Kyle, W.C. McIntosh, Infrasonic tracking of large bubble bursts and ash venting at Erebus Volcano, Antarctica, J. Volcanol. Geotherm. Res. 177 (2008) 661–672.
[7] C.K. Algar, B.P. Boudreau, Transient growth of an isolated bubble in muddy, fine-grained sediments, Geochim. Cosmochim. Acta 73 (2009) 2581–2591.
[8] E.W. Llewellin, M. Manga, Bubble suspension rheology and implications for conduit flow, J. Volcanol. Geotherm. Res. 143 (2005) 205–217.
[9] L. Caricchi, L. Burlini, P. Ulmer, T. Gerya, M. Vassalli, P. Papale, Non-newtonian rheology of crystal-bearing magmas and implications for magma ascent dynamics, Earth Planet. Sci. Lett. 264 (2007) 402–419.
[10] M. Manga, M. Loewenberg, Viscosity of magmas containing highly deformable bubbles, J. Volcanol. Geotherm. Res. 105 (2001) 19–24.
[11] R.P. Chhabra, Bubbles, Drops and Particles in Non-Newtonian Fluids, CRC Press, Technology & Engineering, 1993. 417 p
[12] T. Tsukada, H. Mikami, M. Hozawa, N. Imaishi, Theoretical and experimental studies of the deformation of bubbles in quiescent Newtonian and non-Newtonian liquids, J. Chem. Eng. Japan 23 (2) (1990) 192–198.
[13] D. Funfschilling, H.Z. Li, Effects of the injection period on the rise velocity and shape of a bubble in a non-Newtonian fluid, Chem. Eng. Res. Des. 84 (A10) (2006) 875–883.
[14] C. Málaga, J.M. Rallison, A rising bubble in a polymer solution, J. Non-Newtonian Fluid Mech. 141 (2007) 59–78.
[15] L.G. Leal, J. Skoog, A. Acrivos, On the motion of gas bubbles in a viscoelastic liquid, Can. J. Chem. Eng. 49 (1971) 569–575.
[16] O. Hassager, Negative wake behind bubbles in non-Newtonian liquids, Nature 279 (1979) 402–403.
[17] A. Belmonte, Self-oscillations of a cusped bubble rising through a miscellar solution, Rheol. Acta 39 (2000) 554–559.
[18] N. Handzy, A. Belmonte, Oscillatory rise of bubbles in wormlike miscellar fluids with different microstructures, Phys. Rev. Lett. 92 (12) (2004) 124501.
[19] Y. Kawase, J.J. Ulbrecht, On the abrupt change of velocity of bubbles rising in non-Newtonian liquids, J. Non-Newtonian Fluid Mech. 8 (1981) 203–212.
[20] J.R. Herrera-Velarde, R. Zenit, D. Chehata, B. Mena, The flow of non-Newtonian fluids around bubbles and its connection to the jump discontinuity, J. Non-Newtonian Fluid Mech. 111 (2003) 199–209.
[21] P.G. Saffman, G. Taylor, The penetration of a fluid into a porous medium or Hele-Shaw cell containing a more viscous liquid, Proc. Roy. Soc. Ser. A 245 (1958) 312–329.
[22] P.G. Saffman, Viscous fingering in Hele-Shaw cells, J. Fluid Mech. 173 (1986) 73–94.
[23] D.C. Hong, J.S. Langer, Analytic theory of the selection mechanism in the Saffman-Taylor problem, Phys. Rev. Lett. 56 (19) (1986) 2032–2035.
[24] P. Tabeling, G. Zocchi, A. Libchaber, An experimental study of the Saffman-Taylor instability, J. Fluid Mech. 177 (1987) 67–82.
[25] A. Lindner, D. Bonn, J. Meunier, Viscous fingering in a shear-thinning fluid, Phys. Fluids 12 (2) (2000) 256–261.
[26] A. Lindner, D. Bonn, J. Meunier, Viscous fingering in complex fluids, J. Phys. 12 (2000) A477–A482.
[27] A. Lindner, D. Bonn, E. Corvera Poiré, M. Ben Amar, J. Meunier, Viscous fingering in a non-Newtonian fluid, J. Fluid Mech. 469 (2002) 237–256.
[28] G. Taylor, P.G. Saffman, A note on the motion of bubbles in a Hele-Shaw cell and porous medium, Quart. J. Mech. Appl. Math. 12 (3) (1959) 265–279.

[29] V. Roig, M. Roudet, F. Risso, A.-M. Billet, Dynamics of a high-Reynolds-number bubble rising within a thin gap, J. Fluid Mech. 707 (2012) 444–466.
[30] X. Wang, B. Klaasen, J. Degrève, B. Blanpain, F. Verhaeghe, Experimental and numerical study of buoyancy-driven single bubble dynamics in a vertical Hele-Shaw cell, Phys. Fluids 26 (2014) 123303.
[31] A. Filella, P. Ern, V. Roig, Oscillatory motion and wake of a bubble rising in a thin-gap cell, J. Fluid Mech. 778 (2015) 60–88.
[32] M. Kawaguchi, S. Niga, N. Gou, K. Miyake, Buoyancy-driven path instabilities of bubble rising in simple and polymer solutions of Hele-Shaw cell, J. Phys. Soc. Jpn. 75 (12) (2006) 124401.
[33] R. Zenit, J. Magnaudet, Path instability of rising spheroidal air bubbles: A shape-controlled process, Phys. Fluids 20 (2008) 061702.
[34] H. Kozuka, Y. Ikeda, M. Kawaguchi, Path instabilities of bubble rising in polymer solutions of Hele-Shaw cell, J. Phys. Soc. Jpn. 78 (11) (2009) 114604.
[35] M. Yamamoto, M. Kawaguchi, Differences in path instabilities between a bubble rising in water and in aqueous polymer solution in a Hele-Shaw cell in the transient and steady states, J. Disper. Sci. Technol. 32 (2011) 1445–1451.
[36] W.W. Graessley, S.F. Edwards, Entanglement interactions in polymers and the chain contour concentration, Polymer 22 (1981) 1329–1334.
[37] B. Song, J. Springer, Determination of interfacial tension from the profile of a pendant drop using computer-aided image processing 1. Theoretical, J. Colloid Interf. Sci. 184 (1996) 64–76.
[38] B. Song, J. Springer, Determination of interfacial tension from the profile of a pendant drop using computer-aided image processing 2. Experimental, J. Colloid Interf. Sci. 184 (1996) 77–91.
[39] V. Gauri, K.W. Koelling, Extensional rheology of concentrated poly(ethylene oxide) solutions, Rheol. Acta 36 (1997) 555–567.
[40] R.B. Bird, R.C. Armstrong, O. Hassager, Dynamics of Polymeric Liquids, Wiley, New York, 1987. Vol. I and II
[41] C.W. Macosko, Rheology: Principles, Measurements, and Applications, Wiley-VCH (1994). 568 p
[42] R.K. Gupta, Polymer and Composite Rheology, 2nd ed., 2000. CRC Press, 416 p.
[43] P. Aussillous, D. Quéré, Quick deposition of a fluid on the wall of a tube, Phys. Fluids 12 (10) (2000) 2367–2371.
[44] R.G. Sousa, S. Nogueira, A.M.F.R. Pinto, M.L. Riethmuller, J.B.L.M. Campos, Flow in the negative wake of a Taylor bubble rising in viscoelastic carboxymethylcellulose solutions: particule image velocimetry measurements, J. Fluid Mech. 511 (2004) 217–236.
[45] J.L. White, Dynamics of viscoelastic fluids, melt fracture, and the rheology of fiber spinning, J. Appl. Polym. Sci. 8 (1964) 2339–2357.
[46] J. Dealy, Weissenberg and Deborah numbers – their definition and use, Rheol. Bull. 79 (2) (2010) 14–18.
[47] R.J. Poole, The Deborah and Weissenberg numbers, Rheol. Bull. 53 (2) (2012) 32–39.
[48] A. Lindner, L'instabilité de Saffman-Taylor dans les fluides complexes : relation entre les propriétés rhéologiques et la formation de motifs, Université Paris VI, Paris, 2000. PhD thesis, 194 p.
[49] S. Li, Y. Ma, T. Fu, C. Zhu, H. Li, The viscosity distribution around a rising bubble in shear-thinning non-Newtonian fluids, Braz. J. Chem. Eng. 29 (2) (2012) 265–274.
[50] J.R. Vélez-Cordero, R. Zenit, Bubble cluster formation in shear-thinning inelastic bubbly columns, J. Non-Newtonian Fluid Mech. 166 (2011) 32–41.
[51] J.R. Vélez-Cordero, D. Sámano, P. Yue, J.J. Feng, R. Zenit, Hydrodynamic interaction between a pair of bubbles ascending in shear-thinning inelastic fluids, J. Non-Newtonian Fluid Mech. 166 (2011) 118–132.